ARTICLE Open Access

High-efficiency broadband active metasurfaces via reversible metal electrodeposition

Qizhang Li[1], Sachin Prashant Kulkarni[2], Chenxi Sui[1], Ting-Hsuan Chen[1,3], Gangbin Yan[1], Ronghui Wu[4], Wen Chen[1], Pei-Jan Hung[1], Xubing Wu[1], Tadej Emersic[1], Koray Aydin[2] and Po-Chun Hsu[1]✉

Abstract

Realizing active metasurfaces with substantial tunability is important for many applications but remains challenging due to difficulties in dynamically tuning light-matter interactions at subwavelength scales. Here, we introduce reversible metal electrodeposition as a versatile approach for enabling active metasurfaces with exceptional tunability across a broad bandwidth. As a proof of concept, we demonstrate a dynamic beam-steering device by performing reversible copper (Cu) electrodeposition on a reflective gradient metasurface composed of metal-insulator-metal resonators. By applying different voltages, the Cu atoms can be uniformly and reversibly electrodeposited and stripped around the resonators, effectively controlling the gap-surface plasmon resonances and steering the reflected light. This process experimentally achieved >90% diffraction efficiencies and >60% reflection efficiencies in both specular and anomalous modes, even after thousands of cycles. Moreover, these high efficiencies can be extended from the visible to the near- and mid-infrared regimes, demonstrating the broad versatility of this approach in enabling various active optical and thermal devices with different working wavelengths and bandwidths.

Introduction

Tailoring light-matter interactions at subwavelength scales has garnered tremendous scientific interest and is key to a plethora of transformative technologies such as invisible cloaks[1–3], flat lenses[4–6], advanced waveguides[7,8], and daytime radiative coolers[9–15]. Its great potential has recently been manifested in metasurfaces, which provide a full manipulation of light on the amplitude, phase, and polarization within a subwavelength-structured interface[16–20]. With the promise to achieve the ultimate miniaturization of optical elements, metasurfaces have rapidly advanced to the forefront of optics research over the past decade[21–23]. Furthermore, the emergence of metasurfaces also raises the hope of revolutionizing active optical components for advanced applications that demand ultracompact and lightweight optics, such as augmented/virtual reality glasses and unmanned aerial vehicles[24–43]. Nevertheless, it is still challenging to achieve active metasurfaces with substantial tunability compared to conventional bulky optics like deformable mirrors[44]. Addressing this challenge is essential for active metasurfaces to outperform their bulky counterparts and step further toward commercial success[45–47].

An essential pathway to achieve high-contrast active metasurfaces is to use materials with highly tunable optical properties. Among the most promising candidates are phase change materials, which feature the metal-insulator transition (MIT), capable of creating substantial changes in refractive index[48]. To date, MIT materials such as vanadium dioxide[14,49–53] and conjugated polymers[41,54–56] have demonstrated many successful applications in active optical and thermal devices. However, MIT materials exhibit much lower plasma frequencies in their metallic state compared to metals (e.g., Cu), therefore limiting their optical tunability, especially at short wavelengths[57]. The ideal MIT scenario with the highest accessible optical contrast would be creating metals from a vacuum and making them vanish as desired. Such a scenario is not physically feasible due to the law of mass conservation. Nevertheless, this effect can be mimicked

Correspondence: Po-Chun Hsu (pochunhsu@uchicago.edu)
[1]Pritzker School of Molecular Engineering, University of Chicago, Chicago, IL, USA
[2]Department of Electrical and Computer Engineering, Northwestern University, Evanston, IL, USA
Full list of author information is available at the end of the article

© The Author(s) 2026
Open Access This article is licensed under a Creative Commons Attribution 4.0 International License, which permits use, sharing, adaptation, distribution and reproduction in any medium or format, as long as you give appropriate credit to the original author(s) and the source, provide a link to the Creative Commons licence, and indicate if changes were made. The images or other third party material in this article are included in the article's Creative Commons licence, unless indicated otherwise in a credit line to the material. If material is not included in the article's Creative Commons licence and your intended use is not permitted by statutory regulation or exceeds the permitted use, you will need to obtain permission directly from the copyright holder. To view a copy of this licence, visit http://creativecommons.org/licenses/by/4.0/.

with reversible metal electrodeposition (RME), which allows for the creation and removal of metals on demand, leading to an effective switch between metals and electrolytes[57,58]. In this way, RME achieves gigantic optical contrast across an ultrabroad wavelength range and has enabled a variety of applications, including electrochromic windows[59,60], visible and thermal camouflage[61,62], and tunable radiative cooling systems[63,64]. Though appealing, these demonstrations were mostly done on thin film configurations, and the potential of RME in controlling light-matter interactions with subwavelength structures remains largely underdeveloped[65,66]. Given that RME yields substantial optical contrast, it is of both fundamental and practical interest to explore the feasibility of RME within micro and nanostructures and its ability to control subwavelength light-matter interactions.

In this work, we experimentally explored the capability of RME performed on subwavelength structures for realizing high-contrast active metasurfaces. This concept is showcased by an active beam-steering metasurface with tunable metal-insulator-metal (MIM) resonators controlled by the RME of Cu. The top metal and the middle dielectric layers are structured to form the resonant antennas, whereas the bottom metal serves both as an optical element that reflects the incoming light, and as an electrical component utilized as a highly conductive working electrode to enable high-performance RME. As a result, the Cu atoms can be uniformly and reversibly deposited and stripped around the subwavelength resonators by switching the applied bias. This effectively controls the gap-surface plasmon resonance, leading to high-efficiency dynamic beam steering. Furthermore, such substantial tunability can be achieved across a very broad bandwidth from visible to mid-infrared (IR) ranges. Our results highlight promising opportunities to realize the high-contrast active metasurfaces demanded for emerging optical and thermal applications.

Results

Potential of RME for achieving substantial broadband tunability

Figure 1a illustrates the working principle of leveraging RME to control the subwavelength light-matter interactions of a MIM resonator, which is immersed in an electrolyte with the working and counter electrodes. By applying a negative bias to the working electrode, a layer of high-reflectivity metal is deposited around the resonator, which prevents incident light from entering the resonant cavity and turns off its plasmon resonance. The resonance can be fully recovered by reversing the bias polarity, which dissolves the deposited metal into the electrolyte as metal ions. As shown in Fig. 1b, the effective control of gap-surface plasmon resonances extends from the visible to mid-IR ranges using resonators of different sizes. Such a substantial and broadband tunability of RME can be expected from the gigantic refractive index differences between metals and corresponding electrolytes over a broad bandwidth (Table S1). To further demonstrate the optical tunability potential of RME, we compare it with other representative active materials by calculating their tuning ranges in terms of the single-interface normal-incidence reflectivity, $R = \left|\frac{\tilde{n}-1}{\tilde{n}+1}\right|^2$ where $\tilde{n}$ is the complex refractive index. Specifically, the optical properties of the two states of active materials ($\tilde{n}_1$ and $\tilde{n}_2$) are used to calculate the corresponding reflectivities (R_1 and R_2), as depicted in the inset of Fig. 1c. This is a reasonable standard for comparison as it involves only the material properties (i.e., $\tilde{n}$). The ideal active material should feature $\Delta R = |R_1 - R_2| = 1$, fully suppressing reflection at the interface ($R = 0$) in the initial state and entirely reflecting all the incident light ($R = 1$) as the material property changes. As shown in Fig. 1c, RME stands out from commonly used active materials[24,41,67–78] with its near-unity contrast ($\Delta R \approx 1$) across the entire wavelength range of interest. This promises RME's great potential to achieve active metasurfaces with substantial tunability over an ultrabroad wavelength range.

High-efficiency dynamic beam steering via RME-based active metasurface

To demonstrate the potential of RME-based active metasurfaces, we focus on dynamic beam steering, as achieving high-efficiency beam-steering metasurfaces has been quite challenging due to the limited optical property contrast of active materials (Table S2). As illustrated in Fig. 2a, our metasurface consists of MIM resonator arrays with a trapezoidal shape designed to support broadband resonances[79,80]. In its pristine state, when there is no Cu deposition, these trapezoidal antennas impart a phase gradient to the reflected light along the device surface, causing the reflection angle to deviate from the incident angle and resulting in anomalous reflection[81,82]. The anomalous reflection (corresponding to 1st order diffraction) can be greatly suppressed by the metal electrodeposition, which eliminates the phase gradient and switches the reflected light to the specular direction (0th order). Therefore, an electrically tunable metasurface capable of steering light into different directions is realized by changing the applied bias to reversibly deposit and strip the metal layer.

For experimental demonstration, we specifically designed and fabricated the metasurface to operate at visible wavelengths. With minimum feature sizes on the order of tens of nanometers, a successful demonstration of this active metasurface would validate the practicality of RME in controlling light-matter interactions at nanoscales. The top view of the fabricated metasurface is

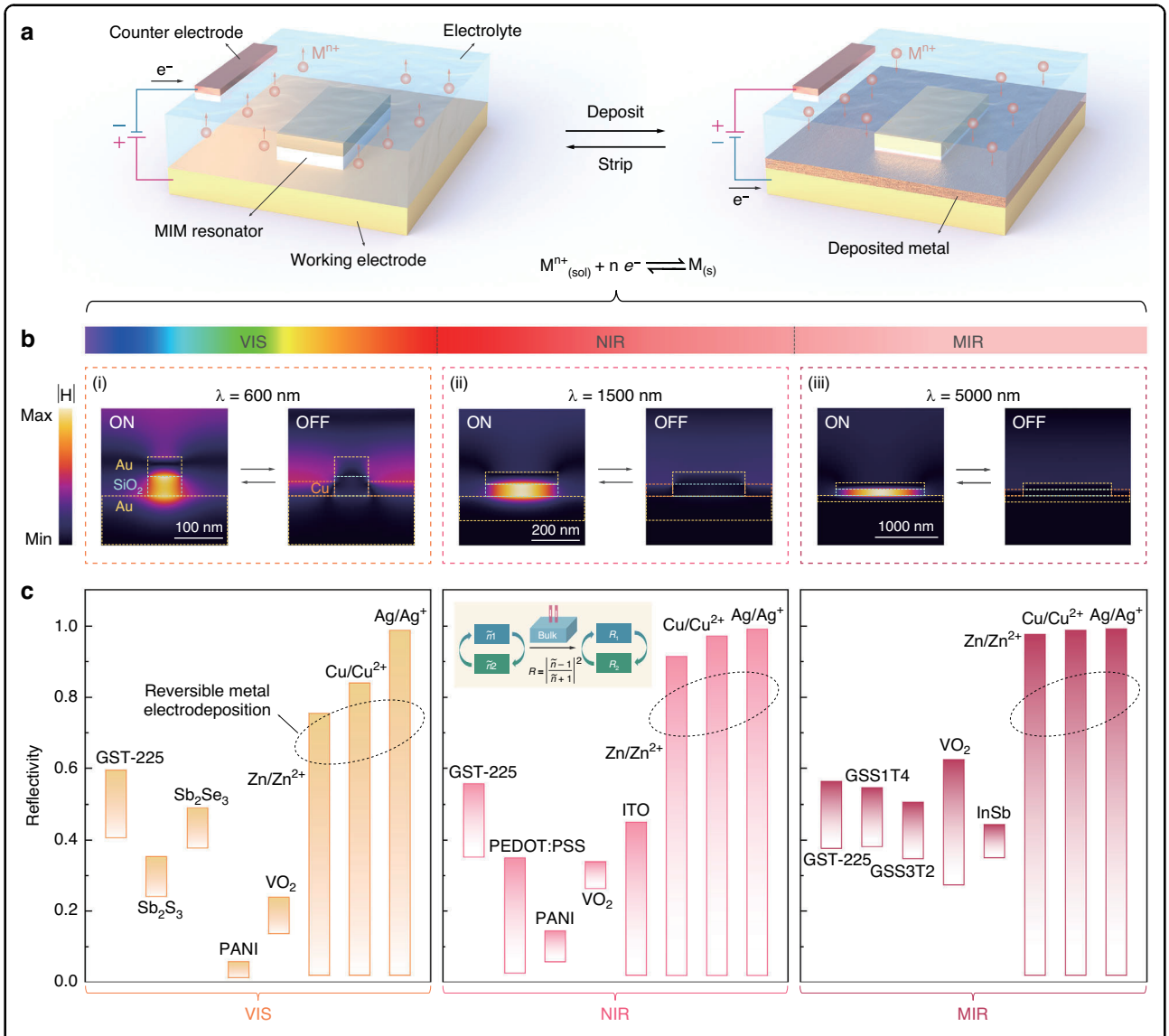

Fig. 1 Concept and potential of active metasurface with substantial broadband tunability enabled by RME. a Schematic of a tunable MIM resonator for dynamic light manipulation via RME. **b** Simulated magnetic field profiles of the MIM resonators controlled by RME at the visible (i), near-IR (ii), and mid-IR (iii) regimes. Simulation details can be found in Fig. S1. **c** Calculated tunable range of single-interface reflectivity for RME and various active materials at different wavelengths, with RME demonstrating the highest tuning potential. Note that materials are grouped by spectral regime, while positions do not correspond to exact wavelengths. The material optical properties used in calculations are provided in Table S1. For the RME of various metals, the optical properties of electrolytes are approximated by those of pure water

shown in Fig. 2b by using scanning electron microscopy (SEM). We used gold (Au) and silicon dioxide (SiO_2) for the metal and insulator components of the MIM resonators, considering their robustness in nanofabrication and RME processes. For the RME operations, we chose Cu as the working metal for its great stability, long durability, and fast switching speed[59,64,83]. By applying a negative voltage to the bottom metal of the metasurface with respect to the counter electrode of Cu foil, a Cu layer was densely and uniformly deposited on the Au substrate as characterized with SEM and energy-dispersive X-ray spectroscopy (EDS) in Fig. 2c. This was further confirmed with cross-sectional scanning transmission electron microscopy (STEM) images as shown in Fig. 2d, e. Such high-quality electrodeposition was enabled by both the high conductivity of the Au electrode and its energy-favorable interface to facilitate the nucleation of Cu[62,64,84]. As indicated by the effective medium theory[85], the dense and continuous deposition morphology is essential to reach the percolation threshold for behaving as a metal

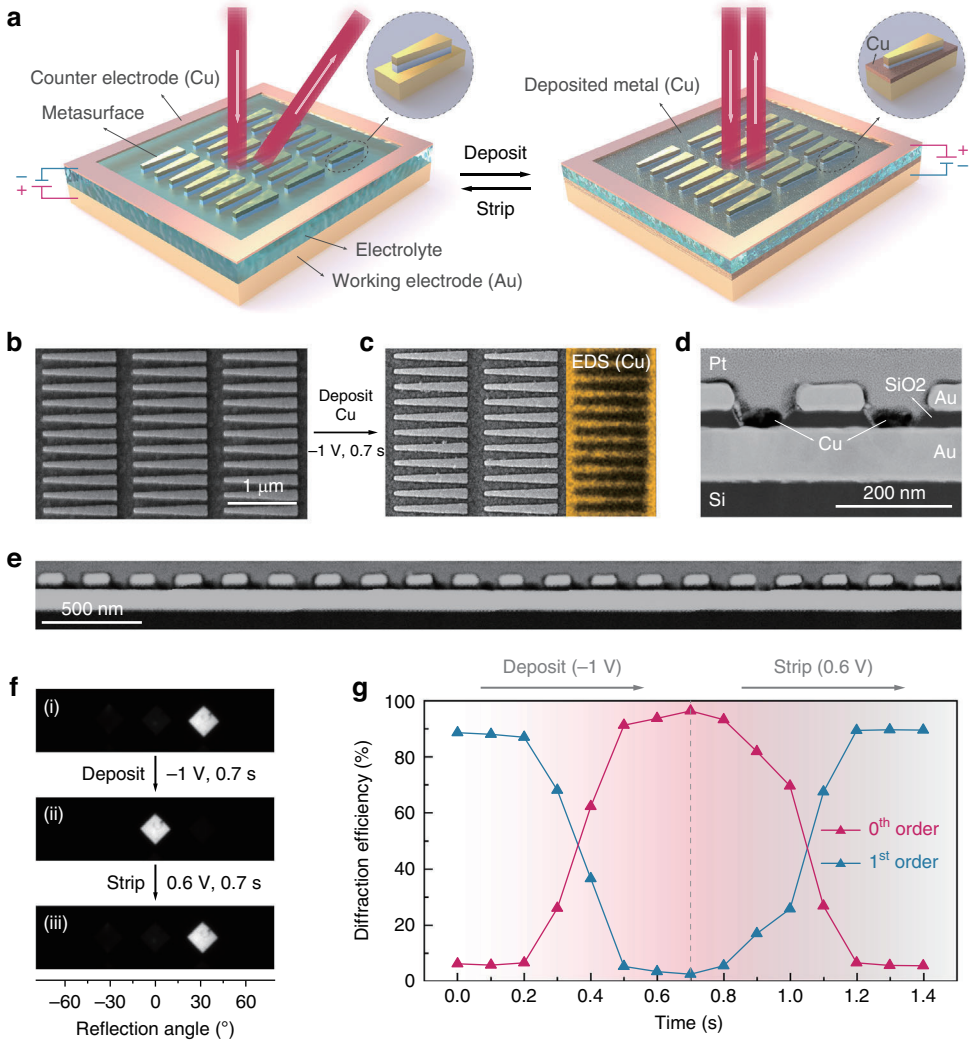

Fig. 2 Active beam-steering metasurface via reversible Cu electrodeposition. a Schematic of the electrochemical device for dynamic beam steering. The device can be electrically switched between the anomalous reflection mode (Cu-stripped, left) and the specular reflection mode (Cu-deposited, right). **b**, **c** Top-view SEM images of the metasurface before (**b**) and after (**c**) Cu electrodeposition. The deposited Cu area is partly highlighted via EDS. **d**, **e** Cross-sectional STEM images of the metasurface deposited with Cu. The sample lamella was prepared using focused ion beam (FIB). **f** Microscope Fourier imaging of the reflected beam profiles for the metasurface as fabricated (i), after Cu electrodeposition (ii), and after stripping Cu (iii). **g** The 0th and 1st order diffraction efficiencies when depositing and stripping Cu with different times. Measurements were performed under normal incidence at a wavelength of 685 nm

film with the desired optical reflectivity[64]. Consequently, the gap-surface plasmon resonance is turned off by the Cu deposition and the metasurface no longer supports anomalous reflection but rather behaves as a reflective mirror with only specular reflection (Fig. 2f). The metasurface fully regains its functionality when applying a positive voltage that quickly oxidizes Cu(s) to Cu^{2+} cations dissolved in the electrolyte (Fig. 2f). Such an on/off switch can be done at a timescale of 500 ms when using an electrolyte with 1 M Cu^{2+}, as illustrated in Fig. 2g. More importantly, with the effective deposition and stripping of Cu at nanoscales, our active metasurface experimentally demonstrated ultrahigh diffraction efficiencies of >90% for both the anomalous and specular reflection modes. Here, the diffraction efficiency, η_d, is defined as the ratio of the light intensity in the desired diffraction order to the total reflected light intensity. This total intensity can be approximated by the sum of all three major diffraction orders (0th and ±1st) as the contributions from higher orders are negligible (Fig. S2). It is noteworthy that achieving high diffraction efficiency is particularly important for metasurfaces to be utilized in practical applications that demand high signal-to-noise ratios (SNR)[86–88].

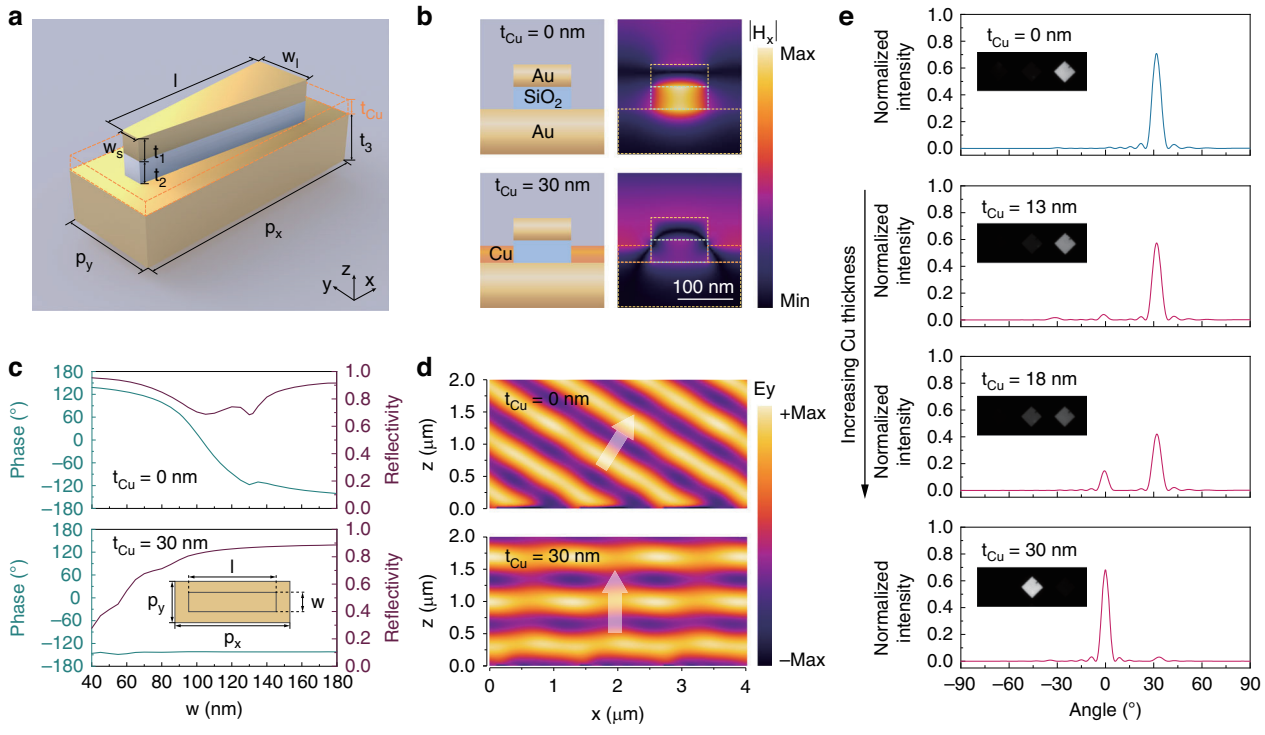

Fig. 3 Mechanisms of the switch between anomalous and specular reflection modes for the RME-based active metasurface. a Schematic of the unit cell with a trapezoidal antenna. For the design operating at visible wavelengths, the geometric parameters are $P_x = 1300\,nm$, $P_y = 220\,nm$, $l = 1056\,nm$, $w_l = 150\,nm$, $w_s = 55\,nm$, $t_1 = 40\,nm$, $t_2 = 40\,nm$, $t_3 = 100\,nm$. **b**–**d** Comparisons between the metasurfaces with and without Cu electrodeposition in terms of the cross-sectional unit-cell schematics and corresponding simulated magnetic fields (**b**), phase and reflectivity profiles for a rectangular antenna as a function of its width w (**c**), and the electric fields of reflected light above the metasurface (**d**). The cross-section mapping is along the center of the unit cell ($P_x/2$). The inset in (**c**) shows a top view of the rectangular antenna unit cell. **e** Simulated far-field intensity profiles of reflected light with increasing Cu thickness, which is normalized to the peak reflection intensity of a silver mirror. Insets are corresponding measured beam profiles. In the simulations, the wavelength of light is 685 nm, and the polarization is along the *y*-axis

Mechanisms of active beam-steering metasurface

The underlying mechanisms of our active metasurface were theoretically studied with full-field electromagnetic simulations using the unit cell depicted in Fig. 3a. In its initial state (prior to Cu deposition), the MIM resonator supports a gap-surface plasmon resonance localized near the center of the antenna when illuminated with 685-nm light, as indicated by the enhanced magnetic field within the MIM cavity (Fig. 3b). With the dramatic phase shift imparted by the MIM resonator, the trapezoidal antenna enables a near-2π phase coverage required for the anomalous reflection response, owing to its gradually increasing width along the antenna which induces different phase shifts (Fig. 3c). This phase gradient imparts an additional wave vector to the normally incident light and leads to anomalously reflected wavefront as shown in Fig. 3d. In great contrast, after depositing only a 30 nm Cu layer around the cavity, the plasmon resonance is significantly suppressed (Fig. 3b), fully eliminating the phase gradient (Fig. 3c). As a result, the reflected light is steered from the anomalous angle to the normal direction (Fig. 3d). It is noteworthy that the reflectivity remains consistently high when switching the beam propagation directions, as indicated by the reflectivity plots in Fig. 3c. This is the foundation to realize dynamic beam steering with high efficiencies without loss of incident optical power.

To further analyze how the reflected light is steered between different directions during electrodeposition, we simulated the far-field intensity profiles for varying Cu thicknesses (Fig. 3e). The simulation results agree well with the experimental observations (Fig. 3e insets), where the same nominal thickness of Cu is deposited. Both theoretical and experimental results demonstrate that, with a 40 nm SiO_2 cavity, a 30 nm Cu layer is sufficient to fully switch the beam propagating direction. This low requirement for deposited Cu thickness is crucial for achieving active metasurfaces with excellent durability and fast switching speeds[89]. In addition, the required deposition thickness can be reduced to 20 nm by optimizing the MIM resonator design with a thinner SiO_2 layer, or even to 10 nm by embedding the bilayer antenna into the Au substrate (Fig. S3 and S4). This indicates great promise for further improving the device performance, such as

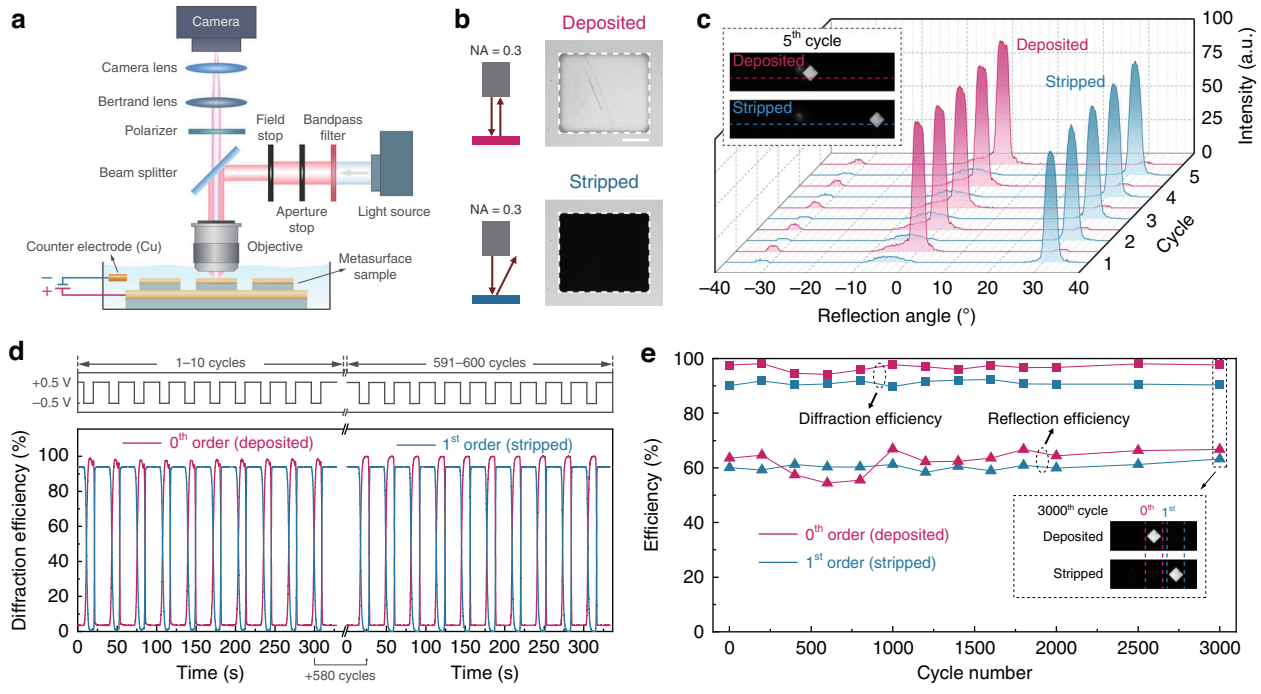

Fig. 4 Experimental demonstration of consistently high-efficiency dynamic beam steering. a Schematic of the microscope setup for characterizing the reflected beam profile. A dipping lens is immersed in the working electrolyte for the in-situ measurements. **b** Microscope images of the metasurface sample in the deposited and stripped states when a 0.3-NA objective is used. The metasurface area is circled with a white dashed line. The scale bar is 100 μm. **c** Line profiles of intensity captured via the Fourier plane imaging for the initial five in-situ cycles. Insets are the camera images for the fifth cycle, and the dashed lines indicate where the intensity profile is extracted. **d** In-situ measurement of the 0th and 1st order diffraction efficiencies in the deposited and stripped states for the 1–10 (left) and 591–600 (right) cycles. The corresponding videos are provided as supplemental auxiliary files. **e** Cycle life test of the active metasurface on the diffraction and reflection efficiencies. The inset shows the Fourier plane images for the deposited and stripped states at the 3000th cycle. The test was done in ex-situ experiments by applying -1 V for 0.7 s in the deposition process and 0.5 V for 10 s for a complete stripping

switching speed, which extends the range of potential applications for RME-based active metasurfaces[43,46].

In-situ and ex-situ characterizations on beam steering performance

To characterize the beam steering performance, we set up a microscopy system, as shown in Fig. 4a. Incident light with a wavelength of 685 nm was generated using a bandpass filter in the path of a white light source. An objective with a small numerical aperture (NA = 0.3) allowed us to clearly observe the distinct difference in the metasurface's appearance between the deposited and stripped states (Fig. 4b). When Cu was deposited on the device, the entire metasurface area (300 × 340 μm^2) appeared as bright as the surrounding flat region. Conversely, when Cu was stripped from the device, the metasurface area became noticeably dark, as most of the light was anomalously reflected to ~30°, beyond the detectable angle range of the 0.3-NA objective (<17.5°).

The angle-resolved quantitative measurement of light intensity was further achieved by Fourier plane imaging[90], a technique that uses the Bertrand lens to project the Fourier transform of the image plane onto the camera, allowing each pixel to correspond to a specific reflection angle (Fig. S5). In this case, a high-NA objective was required to capture reflected light over a wide angular range. For in-situ measurements, we used a 0.8-NA dipping lens immersed in a dilute electrolyte containing 50 mM Cu^{2+}. While using dilute electrolytes decreases the switching speed, it ensures sufficient reflected light intensity for camera detection, compensating for the strong absorption of red light in the Cu^{2+} electrolyte due to the long working distance of the dipping lens (3.3 mm). Figure 4c displays the line profile of the reflected beam intensity for the initial five cycles of the experiments, during which the light was efficiently steered toward different directions. By analyzing the light intensity at different beam spots, we derived the diffraction efficiencies for the 0th and 1st order diffractions in both the deposited and stripped states. As shown in Fig. 4d, both states stably achieved over 90% diffraction efficiencies for up to 600 cycles.

To further explore the reversibility of the device, we conducted a cycle test via ex-situ measurements on both

diffraction and reflection efficiencies at different states. The reflection efficiency, η_r, is defined as the intensity of the targeted diffracted light normalized to the incident light intensity, which is approximated by the reflection from a silver mirror. As shown in Fig. 4e, the RME-based active metasurface consistently achieved ~60% reflection efficiency and ~90% diffraction efficiency without degradation even after 3000 cycles. This excellent cyclability is largely attributed to the use of the Au back reflector as the working electrode, which is ideal for RME due to its high conductivity and low lattice mismatch with Cu[91]. Our findings highlight the potential of RME to enable active metasurfaces with exceptional optical performance, high stability, and long-term durability. We note that all optical characterizations in this work, except for the in-situ experiments, were conducted under dry conditions, without electrolyte present during measurement. This ensures a clearer demonstration of the optical modulation ability due to the Cu deposition and removal via RME operations, without interference from variations in electrolyte composition, concentration, or thickness. Although the electrolyte might greatly affect the overall reflection intensity at specific wavelengths due to its absorption, the diffraction efficiencies can remain well preserved, as demonstrated in Fig. 4d, e. Accordingly, to maintain consistency with the experimental conditions, air was adopted as the surrounding medium in all simulations presented in this work, unless otherwise specified.

Broadband demonstration of RME-based active metasurfaces

The synergy of Cu as a Drude metal and the trapezoidal antenna design suggests substantial broadband capabilities for our active beam-steering metasurfaces. To explore this potential in the visible and near-IR regimes, we employed a custom-built angle-resolved spectroscopy system to characterize the anomalously reflected light, as depicted in Fig. 5a[79,92]. Subsequently, the diffraction and reflection efficiencies for different diffraction orders were determined with a microscope-based spectroscopy system. For the visible regime, we continued using the aforementioned metasurface design and investigated its broadband performance at other visible wavelengths. As plotted in Figs. 5b and S6, extraordinary optical performance ($\eta_d \approx 90\%$ and $\eta_r \approx 60\%$) was observed for both deposited and stripped states across a 100-nm-wide wavelength range from 610 to 710 nm. This broadband tunability arises from the leverage of trapezoidal antennas (Fig. S7) and the substantial optical contrast provided by the RME of Cu (Fig. 1c). We note that Cu is less suitable for devices working at shorter visible wavelengths due to its absorptive nature in that region, and RME of silver or aluminum can be more effective[62,93]. For the near-IR demonstration, we redesigned and fabricated the metasurface with larger feature sizes to accommodate wavelengths up to 800 nm, considering the experimental setup availability. The measurement results, also shown in Fig. 5b, consistently demonstrated high efficiencies across this extended wavelength range.

For the mid-IR wavelengths, the angle-resolved reflectance spectrum was measured with an IR ellipsometer as shown in Fig. 5c. Due to the limitations of the instrument on detection angles, we designed the mid-IR metasurface considering a tilted incidence angle of 32° and conducted measurements at reflection angles of 32° and above. In this case, the 0th and 1st order diffracted light with a 3 μm wavelength were predicted to feature reflection angles of 32° and 50°, respectively, according to the generalized Snell's law[81], which was confirmed by the measurements (Fig. S8). The reflection efficiencies of the 0th and 1st order diffractions for both deposited and stripped states are shown in Fig. 5d, where $\eta_r \approx 60\%$ is consistently achieved over a broad wavelength range from 2.6 to 3.6 μm. Although the diffraction efficiencies at these wavelengths could not be determined due to the difficulties in measuring the -1st order diffraction, one can still expect considerably high values from the distinct intensity contrast between 0th and 1st orders.

Using the measured beam-steering efficiencies, we determined the SNR of the RME-based metasurfaces, a key figure of merit for real-world applications that require the output signal to be distinguishable from the background[26]. The SNR is the intensity ratio between the dominant diffraction order and the second-highest one[26]. Since the active metasurfaces exhibit different SNRs during switching, the smallest value among different states is considered, as it represents the performance limit of active devices. Our results show that RME-based metasurfaces consistently exhibit higher SNR from visible to mid-IR ranges compared to many other active-material systems (Fig. 5e), in line with the optical contrast comparison in Fig. 1c. While the reflection efficiencies might be limited in the mid-IR regime due to the electrolyte absorption, the high diffraction efficiencies and SNR would remain unaffected. We anticipate the great potential of RME-based metasurfaces could intrigue further research efforts to demonstrate more possibilities such as faster switching speed[24,33,94–97], multiple-angle steering[26,98–100], high-performance transmissive counterparts[36,39,41,101,102], and novel functionalities[43,103–105].

Discussion

We have demonstrated the remarkable potential of reversible metal electrodeposition for enabling active metasurfaces with exceptional broadband tunability. Leveraging the ideal optical contrast provided by RME, we experimentally realized active beam-steering metasurfaces with reflection efficiencies of >60% and diffraction

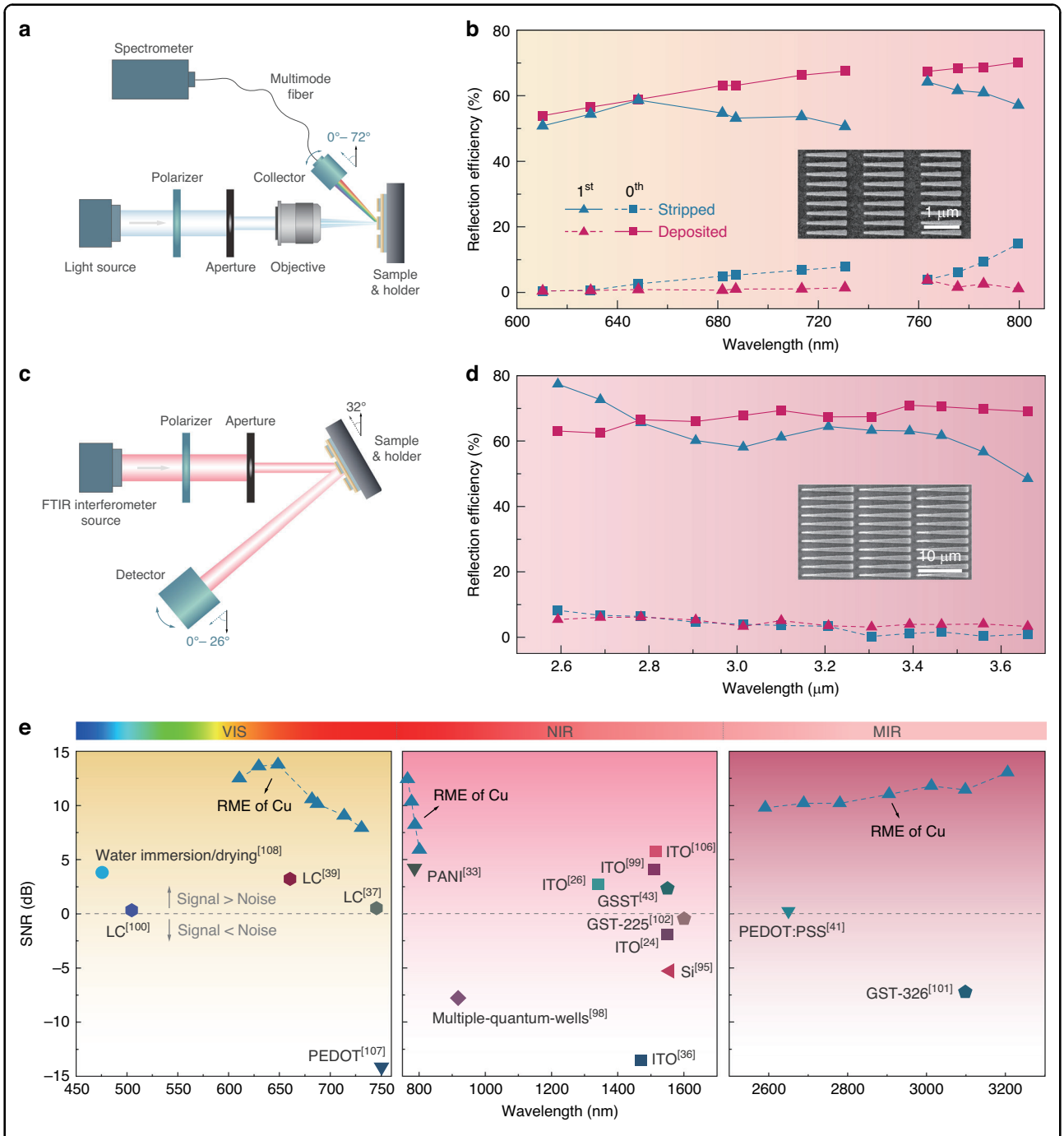

Fig. 5 RME-based metasurfaces with broadband dynamic beam-steering capability. a, **b** Schematic of the angle-resolved spectroscopy system (**a**) and the ex-situ measured reflection efficiencies in the visible and near-IR ranges (**b**). Inset is the SEM image of the near-IR sample. **c**, **d** Schematic of the ellipsometer setup (**c**) and the ex-situ measured reflection efficiencies in the mid-IR range (**d**). Inset is the SEM image of the mid-IR sample. **e** Accessible SNR of the RME-based metasurfaces and other up-to-date beam-steering devices working at different wavelengths[24,26,33,36,37,39,41,43,95,98–102,106–108]

efficiencies of >90%, leading to remarkable SNRs up to ~15 dB. Furthermore, such high performance extends well across the visible, near-IR, and mid-IR ranges using different-sized metasurfaces based on the same design principle. This was accomplished through a plasmonic metasurface design that combines both photonic and electrochemical considerations, utilizing the metal back reflector of the antennas as a desirable working electrode for RME operation. Consequently, Cu atoms can be uniformly and reversibly electrodeposited and stripped at the

nanoscale during switching, leading to exceptional optical performance and electrochemical sustainability, as validated by the ex- and in-situ experiments. This work opens opportunities for dynamic control of light at subwavelength scales, facilitating the development of active optical and thermal metadevices with ultrahigh efficiencies.

Materials and methods

Numerical simulations

The numerical simulations of the metasurfaces are performed with the commercial software of COMSOL version 5.6. We apply periodic boundary conditions to the x- and y-directions at the surface edges of the 3D unit cell model, which is normally illuminated by an incident plane wave with a polarization along the y-direction. The perfectly matched layer is added to both the top and bottom ends of the unit cell for convergence purposes. The refractive index of Au and SiO_2 in simulations is obtained from the ellipsometry measurements, while that of Cu is adopted from the literature[73].

Fabrication of metasurfaces for operating in the visible and near-IR regimes

The metasurfaces with nanoscale feature sizes were fabricated using electron-beam lithography. We started with covering a glass substrate with a 5 nm chromium (Cr) adhesive layer and a 100 nm Au layer using electron-beam evaporation (AJA e-beam Evaporator). The sample was primed with HMDS for 5 min, spin-coated with a 950 PMMA A4 resist at a rate of 6000 rpm for 1 min, baked at 180 °C for 5 min, and then exposed in the Raith EBPG5200 E-Beam lithography system operated at 100 kV with a dose of 700 μC/cm^2. The sample was developed in a MIBK/IPA (1:3) solvent for 2 min at room temperature and then rinsed with IPA and DI water for 1 min each. The antenna pattern was formed by sequentially depositing SiO_2 and Au using electron-beam evaporation. Before and after the SiO_2 deposition, 2 nm of Cr was deposited to enhance the antenna adhesion. Note that a 3 nm layer of SiO_2 was deposited on top of the Au antenna to prevent the undesired Cu electrodeposition. Afterwards, the sample was lifted off by soaking in acetone at 60 °C for 15 min and then sonicating for 10 s. The sample was then subjected to O_2 plasma processing to completely remove the residual resist.

Fabrication of metasurfaces for operating in the mid-IR regimes

The micro-size metasurfaces were fabricated by a typical photolithography process. A silicon wafer substrate was covered with a 5 nm Cr layer and a 100 nm Au film using electron-beam evaporation. The substrate was primed with HMDS for 5 min and then spin-coated with a negative photoresist (AZ nLOF 2020) at 4000 rpm for 45 s. Afterwards, the sample was baked at 110 °C for 1 min and then exposed to a 375 nm laser source in the Heidelberg MLA150 lithography system with a dose of 260 mJ/cm^2. The exposed sample was further baked at 110 °C for 1 min, developed in the AZ 300 MIF developer for 1 min, and rinsed with DI water for 1 min. The subsequent processes and instruments are the same as those used in the electron-beam lithography, including the deposition of antenna materials and the lift-off process.

Electrochemical setup

The electrolyte consisted of 1 M $Cu(ClO_4)_2$, 1 M $LiClO_4$, and 20 mM $HClO_4$. $Cu(ClO_4)_2$ was used because ClO_4^- is the desirable anion for aqueous reversible Cu electrodeposition that suppresses the side reactions (i.e., forming insoluble Cu complexes)[83]. $LiClO_4$ serves as the supporting electrolyte to increase solution conductivity, and the $HClO_4$ prevents the deposition of insoluble Cu_2O complexes[83]. The electrochemical experiments were conducted with the VMP3 potentiostat (BioLogic) under constant potential conditions. The experiments were carried out with the 2-electrode system where the metasurface served as the working electrode and the Cu foil was the counter electrode.

Optical measurements with a microscopy system

The microscopy system (Fig. 4a) was built upon the Olympus BX53 microscope, which could provide the visualization of the dynamic beam steering towards different reflected angles. A white LED light source was used for illumination, filtered by a bandpass filter at 685 nm with a bandwidth of 10 nm (AVR Optics). The aperture stop in the Köhler illumination tube was used for better collimation of light, and the field stop for limiting the size of the illuminating area. We note that the diamond shape of the beam spot arose from the shape of the aperture stop that we used. The desired polarization of the light was achieved by a polarizer after the reflected light was collected with the objective. The Fourier plane imaging was realized by using the Bertrand lens, a standard lens placed in between the objective and the camera lens. In the ex-situ experiments, two objectives (Olympus, 10×, NA = 0.3; Olympus, 100×, NA = 0.9) were used for different imaging purposes as illustrated in the main text. The dipping objective (Leica, 40×, NA = 0.8) was used for the in-situ experiments.

Broadband beam-steering characterization for visible and near-IR wavelengths

The intensity of the anomalously reflected beam at different visible and near-IR wavelengths was measured with a custom-built angle-resolved spectroscopy system (Fig. 5a). The light from a broadband halogen lamp source

was collimated and polarized before entering the aperture to achieve a desired incident beam feature. The light was focused on the sample using the 4× Nikon achromatic objective and then collected at different reflection angles by another objective installed on a rotatable stage. With this setup, the accessible range of the reflection angles was from 18° to 90°. By using the multimode fiber, the collected light was then coupled to a spectrometer system, which consists of a 303 mm focal-length monochromator and an Andor−Newton electron multiplication CCD.

To further characterize the reflection and diffraction efficiencies of different diffraction orders, we employed a microscope-based spectroscopy system (HORIBA SMS Microspectroscopy). This instrument utilizes a series of mirror arrays to collimate and shrink down the beam spot size of a tungsten halogen white light source (Ocean Optics, 4.7 mW, 360-2400 nm). The 0th order reflection light intensity was measured by using a 0.3-NA objective which can eliminate the higher-order reflections. By using a silver mirror to characterize the incident light intensity, we then derived the 0th order reflection efficiency. The total reflection efficiency (approximated to the sum of 0th and ±1st orders) was similarly characterized but with a 0.9-NA objective. In combination with the measurement results from the angle-resolved spectroscopy system, we could then distinguish the reflection efficiency of 0th, +1st, and −1st orders, respectively.

Broadband beam-steering characterization for mid-IR wavelengths

The mid-IR measurements were performed on the IR-VASE ellipsometer (J.A. Woollam), which includes a Fourier transform infrared (FTIR) spectroscopy interferometer light source and a deuterated triglycine sulfate (DTGS) detector installed on a rotatable stage (Fig. 5c). Due to the limitation of the detectable reflection angles, the measurements were conducted with a tilted incident angle of 32°, and the reflected light was collected starting from 32° to larger reflection angles. During the experiments, the iris of the light source was turned to the smallest value (~1 mm) to yield a small beam spot to be fully covered in the patterned area (13 × 14 mm^2). An evaporated Au mirror was used as a reference sample for calculating reflection efficiency, which was measured at 32° for both incident and reflection angles.

Scanning transmission electron microscopy (STEM) characterization

The metasurface samples for STEM characterization are fabricated with a substrate of a highly boron-doped silicon wafer (University wafer, #1319) rather than a glass slide for accessing overall high conductivity. To achieve cross-section imaging, we first made a lamella of the metasurface sample using a focused ion beam (FIB) system (ThermoFisher Helios 5CX (cryo) FIB-SEM). The lamella was prepared via the standard lift-out procedure, which includes using a gas injection system to coat the target area with a protective layer of platinum (Pt). Specifically, the Pt layer consisted of a ~300 nm electron-beam-deposited layer (5 kV, 1.4 nA) and a ~4.0 μm ion-beam-deposited layer (30 kV, 0.23 nA). An approximately 12 × 1.5 × 5.0 μm section was cut off from the patterned area using gallium (Ga) ion beams and attached to a Cu half grid using the EasyLift micromanipulator. The lamella was thinned on both sides (initially at 30 kV, 0.78 nA, then at 16 kV, 240 pA, and 5 kV, 47 pA) and then cleaned (at 2 kV, 24 pA) with Ga ion beams, which yielded a ~70 nm thick lamella. Afterwards, the STEM imaging of the lamella was done on the aberration-corrected JEOL ARM200CF with a cold field emission source operated at 200 kV. The STEM images were obtained with the high-angle annular dark-field detector (90-270 mrad). Both the FIB and STEM processes were done with the instruments at the University of Illinois at Chicago.

Acknowledgements
This work made use of the shared facilities in the Searle Cleanroom and the Pritzker Nanofabrication Facility, part of the Pritzker School of Molecular Engineering at the University of Chicago, which is supported by Soft and Hybrid Nanotechnology Experimental (SHyNE) Resource (NSF-ECCS-2025633), a node of the National Science Foundation's National Nanotechnology Coordinated Infrastructure (RRID: SCR_022955). Parts of this work were carried out with the ThermoFisher Helios 5CX (cryo)FIB-SEM instrument in the Electron Microscopy Core of the University of Illinois at Chicago's Research Resources Center, which received support from the University of Illinois at Chicago, Northwestern University, and ARO (W911NF2110052). This work used the JEOL ARM200CF in the Electron Microscopy Core, Research Resources Center at the University of Illinois at Chicago. Q.L. acknowledges Wook Jun Nam for the help in the nanofabrication process and Zhe Cheng for the help with the optical microscope characterization.

Author details
[1]Pritzker School of Molecular Engineering, University of Chicago, Chicago, IL, USA. [2]Department of Electrical and Computer Engineering, Northwestern University, Evanston, IL, USA. [3]Thomas Lord Department of Mechanical Engineering and Materials Science, Duke University, Durham, NC, USA. [4]School of Materials Science and Engineering, Nanyang Technological University, Singapore, Singapore

Author contributions
P.-C.H. and Q.L. conceived the idea. Q.L. performed the device design and simulations, fabrications, electrochemical experiments, characterizations, and corresponding data analyses. S.P.K. and K.A. conducted the angle-resolved spectroscopy measurements, C.S. assisted with the electrochemical experiments, T.-H.C. and X.W. helped with the ellipsometer measurements, G.Y. carried out the lamella preparation using FIB, STEM, and EDS characterizations, R.W. and P.-J.H. assisted with sample preparation, W.C. helped with the e-beam lithography, and T.E. contributed to the Fourier plane imaging. Q.L. and P.-C.H. wrote the manuscript with input from all co-authors.

Funding
The project was supported by the startup fund from the Pritzker School of Molecular Engineering at the University of Chicago and the National Science Foundation (Electrical, Communications and Cyber Systems award no. 2324286). K.A. acknowledges support from the Air Force Office of Scientific Research under award number FA9550-22-1-0300.

Data availability
All data needed to evaluate the conclusions in the paper are present in the paper and/or the Supplementary Materials.

Conflict of interest
The authors declare no competing interests.

Supplementary information The online version contains supplementary material available at https://doi.org/10.1038/s41377-025-02136-x.

Received: 12 May 2025 Revised: 26 October 2025 Accepted: 12 November 2025
Published online: 03 January 2026

References

1. Pendry, J. B., Schurig, D. & Smith, D. R. Controlling electromagnetic fields. *Science* **312**, 1780–1782 (2006).
2. Ergin, T. et al. Three-dimensional invisibility cloak at optical wavelengths. *Science* **328**, 337–339 (2010).
3. Ni, X. J. et al. An ultrathin invisibility skin cloak for visible light. *Science* **349**, 1310–1314 (2015).
4. Parimi, P. V. et al. Imaging by flat lens using negative refraction. *Nature* **426**, 404 (2003).
5. Aieta, F. et al. Multiwavelength achromatic metasurfaces by dispersive phase compensation. *Science* **347**, 1342–1345 (2015).
6. Arbabi, A. et al. Subwavelength-thick lenses with high numerical apertures and large efficiency based on high-contrast transmitarrays. *Nat. Commun.* **6**, 7069 (2015).
7. Bozhevolnyi, S. I. et al. Channel plasmon subwavelength waveguide components including interferometers and ring resonators. *Nature* **440**, 508–511 (2006).
8. Li, Z. Y. et al. Controlling propagation and coupling of waveguide modes using phase-gradient metasurfaces. *Nat. Nanotechnol.* **12**, 675–683 (2017).
9. Rephaeli, E., Raman, A. & Fan, S. H. Ultrabroadband photonic structures to achieve high-performance daytime radiative cooling. *Nano Lett.* **13**, 1457–1461 (2013).
10. Raman, A. P. et al. Passive radiative cooling below ambient air temperature under direct sunlight. *Nature* **515**, 540–544 (2014).
11. Hsu, P. C. et al. Radiative human body cooling by nanoporous polyethylene textile. *Science* **353**, 1019–1023 (2016).
12. Zhai, Y. et al. Scalable-manufactured randomized glass-polymer hybrid metamaterial for daytime radiative cooling. *Science* **355**, 1062–1066 (2017).
13. Mandal, J. et al. Hierarchically porous polymer coatings for highly efficient passive daytime radiative cooling. *Science* **362**, 315–319 (2018).
14. Tang, K. C. et al. Temperature-adaptive radiative coating for all-season household thermal regulation. *Science* **374**, 1504–1509 (2021).
15. Wu, R. H. et al. Spectrally engineered textile for radiative cooling against urban heat islands. *Science* **384**, 1203–1212 (2024).
16. Kildishev, A. V., Boltasseva, A. & Shalaev, V. M. Planar photonics with metasurfaces. *Science* **339**, 1232009 (2013).
17. Yu, N. F. & Capasso, F. Flat optics with designer metasurfaces. *Nat. Mater.* **13**, 139–150 (2014).
18. Zhang, L. et al. Advances in full control of electromagnetic waves with metasurfaces. *Adv. Opt. Mater.* **4**, 818–833 (2016).
19. Krasnok, A., Tymchenko, M. & Alù, A. Nonlinear metasurfaces: a paradigm shift in nonlinear optics. *Mater. Today* **21**, 8–21 (2018).
20. Shaltout, A. M., Shalaev, V. M. & Brongersma, M. L. Spatiotemporal light control with active metasurfaces. *Science* **364**, eaat3100 (2019).
21. Schulz, S. A. et al. Roadmap on photonic metasurfaces. *Appl. Phys. Lett.* **124**, 260701 (2024).
22. Kuznetsov, A. I. et al. Roadmap for optical metasurfaces. *ACS Photonics* **11**, 816–865 (2024).
23. Ha, S. T. et al. Optoelectronic metadevices. *Science* **386**, eadm7442 (2024).
24. Huang, Y. W. et al. Gate-tunable conducting oxide metasurfaces. *Nano Lett.* **16**, 5319–5325 (2016).
25. Park, J. et al. Dynamic reflection phase and polarization control in metasurfaces. *Nano Lett.* **17**, 407–413 (2017).
26. Park, J. et al. All-solid-state spatial light modulator with independent phase and amplitude control for three-dimensional LiDAR applications. *Nat. Nanotechnol.* **16**, 69–76 (2021).
27. Kaissner, R. et al. Electrochemically controlled metasurfaces with high-contrast switching at visible frequencies. *Sci. Adv.* **7**, eabd9450 (2021).
28. Ko, B. et al. Tunable metasurfaces via the humidity responsive swelling of single-step imprinted polyvinyl alcohol nanostructures. *Nat. Commun.* **13**, 6256 (2022).
29. Moon, C. W., Kim, Y. & Hyun, J. K. Active electrochemical high-contrast gratings as on/off switchable and color tunable pixels. *Nat. Commun.* **13**, 3391 (2022).
30. Yoon, J. et al. Chemically and geometrically programmable photoreactive polymers for transformational humidity-sensitive full-color devices. *Nat. Commun.* **15**, 6470 (2024).
31. Ko, B. et al. Hydrogels for active photonics. *Microsyst. Nanoeng.* **10**, 1 (2024).
32. Kang, D. et al. Liquid crystal-integrated metasurfaces for an active photonic platform. *Opto-Electron. Adv.* **7**, 230216 (2024).
33. Lu, W. Z. et al. Active Huygens' metasurface based on in-situ grown conductive polymer. *Nanophotonics* **13**, 39–49 (2024).
34. Doshi, S. et al. Electrochemically mutable soft metasurfaces. *Nat. Mater.* **24**, 205–211 (2025).
35. Jung, C., Lee, E. & Rho, J. The rise of electrically tunable metasurfaces. *Sci. Adv.* **10**, eado8964 (2024).
36. Howes, A. et al. Dynamic transmission control based on all-dielectric Huygens metasurfaces. *Optica* **5**, 787–792 (2018).
37. Komar, A. et al. Dynamic beam switching by liquid crystal tunable dielectric metasurfaces. *ACS Photonics* **5**, 1742–1748 (2018).
38. Cong, L. Q. et al. All-optical active THz metasurfaces for ultrafast polarization switching and dynamic beam splitting. *Light Sci. Appl.* **7**, 28 (2018).
39. Li, S. Q. et al. Phase-only transmissive spatial light modulator based on tunable dielectric metasurface. *Science* **364**, 1087–1090 (2019).
40. Zhang, F. et al. Multistate switching of photonic angular momentum coupling in phase-change metadevices. *Adv. Mater.* **32**, 1908194 (2020).
41. Karst, J. et al. Electrically switchable metallic polymer nanoantennas. *Science* **374**, 612–616 (2021).
42. Jin, Y. et al. Electrochemically driven dynamic plasmonics. *Adv. Photonics* **3**, 044002 (2021).
43. Zhang, Y. F. et al. Electrically reconfigurable non-volatile metasurface using low-loss optical phase-change material. *Nat. Nanotechnol.* **16**, 661–666 (2021).
44. Bifano, T. MEMS deformable mirrors. *Nat. Photonics* **5**, 21–23 (2011).
45. Jung, C. et al. Metasurface-driven optically variable devices. *Chem. Rev.* **121**, 13013–13050 (2021).
46. Jeon, N. et al. Electrically tunable metasurfaces: from direct to indirect mechanisms. *N. J. Phys.* **24**, 075001 (2022).
47. Gu, T. et al. Reconfigurable metasurfaces towards commercial success. *Nat. Photonics* **17**, 48–58 (2023).
48. Ko, J. H. et al. A review of tunable photonics: Optically active materials and applications from visible to terahertz. *iScience* **25**, 104727 (2022).
49. Dicken, M. J. et al. Frequency tunable near-infrared metamaterials based on VO_2 phase transition. *Opt. Express* **17**, 18330–18339 (2009).
50. Kocer, H. et al. Thermal tuning of infrared resonant absorbers based on hybrid gold-VO_2 nanostructures. *Appl. Phys. Lett.* **106**, 161104 (2015).
51. Kim, Y. et al. Phase modulation with electrically tunable vanadium dioxide phase-change metasurfaces. *Nano Lett.* **19**, 3961–3968 (2019).
52. Howes, A. et al. Optical limiting based on huygens' metasurfaces. *Nano Lett.* **20**, 4638–4644 (2020).
53. Li, Q. Z. et al. Thin-film radiative thermal diode with large rectification. *Phys. Rev. Appl.* **16**, 014069 (2021).
54. Chen, S. Z. et al. Conductive polymer nanoantennas for dynamic organic plasmonics. *Nat. Nanotechnol.* **15**, 35–40 (2020).
55. Karki, A. et al. Electrical tuning of plasmonic conducting polymer nanoantennas. *Adv. Mater.* **34**, 2107172 (2022).
56. Chen, T. H. et al. A kirigami-enabled electrochromic wearable variable-emittance device for energy-efficient adaptive personal thermoregulation. *PNAS Nexus* **2**, pgad165 (2023).
57. Li, Q. Z., Chen, T. H. & Hsu, P. C. Use electrochemistry to charge the next dynamic thermal metamaterials. *Energy* **3**, 100108 (2024).
58. Tao, X. et al. Reversible metal electrodeposition devices: an emerging approach to effective light modulation and thermal management. *Adv. Opt. Mater.* **9**, 2001847 (2021).

59. Barile, C. J. et al. Dynamic windows with neutral color, high contrast, and excellent durability using reversible metal electrodeposition. *Joule* **1**, 133–145 (2017).
60. Strand, M. T. et al. Polymer inhibitors enable >900 cm2 dynamic windows based on reversible metal electrodeposition with high solar modulation. *Nat. Energy* **6**, 546–554 (2021).
61. Wang, G. P. et al. Mechanical chameleon through dynamic real-time plasmonic tuning. *ACS Nano* **10**, 1788–1794 (2016).
62. Li, M. Y. et al. Manipulating metals for adaptive thermal camouflage. *Sci. Adv.* **6**, eaba3494 (2020).
63. Rao, Y. F. et al. Ultra-wideband transparent conductive electrode for electrochromic synergistic solar and radiative heat management. *ACS Energy Lett.* **6**, 3906–3915 (2021).
64. Sui, C. et al. Dynamic electrochromism for all-season radiative thermoregulation. *Nat. Sustain.* **6**, 428–437 (2023).
65. Jin, Y. et al. Electrical dynamic switching of magnetic plasmon resonance based on selective lithium deposition. *Adv. Mater.* **32**, 2000058 (2020).
66. Zhang, S. T. et al. Reversible electrical switching of nanostructural color pixels. *Nanophotonics* **12**, 1387–1395 (2023).
67. Zhang, Y. F. et al. Broadband transparent optical phase change materials for high-performance nonvolatile photonics. *Nat. Commun.* **10**, 4279 (2019).
68. Derkaoui, I. et al. VO_2 thin films for smart windows: numerical study of the optical properties and performance improvement. *J. Phys.: Conf. Ser.* **1292**, 012010 (2019).
69. Delaney, M. et al. A new family of ultralow loss reversible phase-change materials for photonic integrated circuits: Sb_2S_3 and Sb_2Se_3. *Adv. Funct. Mater.* **30**, 2002447 (2020).
70. Liu, H. L. et al. Rewritable color nanoprints in antimony trisulfide films. *Sci. Adv.* **6**, eabb7171 (2020).
71. Barker, A. S. Jr., Verleur, H. W. & Guggenheim, H. J. Infrared optical properties of vanadium dioxide above and below the transition temperature. *Phys. Rev. Lett.* **17**, 1286–1289 (1966).
72. Hale, G. M. & Querry, M. R. Optical constants of water in the 200-nm to 200-μm wavelength region. *Appl. Opt.* **12**, 555–563 (1973).
73. Ordal, M. A. et al. Optical properties of fourteen metals in the infrared and far infrared: Al, Co, Cu, Au, Fe, Pb, Mo, Ni, Pd, Pt, Ag, Ti, V, and W. *Appl. Opt.* **24**, 4493–4499 (1985).
74. Querry, M. R. Optical constants of minerals and other materials from the millimeter to the ultraviolet (U.S. Army Report CRDEC-CR-88009, 1987).
75. Barbero, C. & Kötz, R. Nanoscale dimensional changes and optical properties of polyaniline measured by in situ spectroscopic ellipsometry. *J. Electrochem. Soc.* **141**, 859–865 (1994).
76. Michel, A. K. U. et al. Using low-loss phase-change materials for mid-infrared antenna resonance tuning. *Nano Lett.* **13**, 3470–3475 (2013).
77. Yang, H. U. et al. Optical dielectric function of silver. *Phys. Rev. B* **91**, 235137 (2015).
78. Zheng, J. J. et al. GST-on-silicon hybrid nanophotonic integrated circuits: a non-volatile quasi-continuously reprogrammable platform. *Opt. Mater. Express* **8**, 1551–1561 (2018).
79. Li, Z. Y. et al. Visible-frequency metasurfaces for broadband anomalous reflection and high-efficiency spectrum splitting. *Nano Lett.* **15**, 1615–1621 (2015).
80. Li, Z. Y. et al. Ultrawide angle, directional spectrum splitting with visible-frequency versatile metasurfaces. *Adv. Opt. Mater.* **4**, 953–958 (2016).
81. Yu, N. F. et al. Light propagation with phase discontinuities: Generalized laws of reflection and refraction. *Science* **334**, 333–337 (2011).
82. Sun, S. et al. High-efficiency broadband anomalous reflection by gradient meta-surfaces. *Nano Lett.* **12**, 6223–6229 (2012).
83. Hernandez, T. S. et al. Electrolyte for improved durability of dynamic windows based on reversible metal electrodeposition. *Joule* **4**, 1501–1513 (2020).
84. Yan, K. et al. Selective deposition and stable encapsulation of lithium through heterogeneous seeded growth. *Nat. Energy* **1**, 16010 (2016).
85. Cai, W. S. & Shalaev, V. Optical Metamaterials: Fundamentals and Applications (New York: Springer, 2010).
86. Slobozhanyuk, A. P. et al. Enhancement of magnetic resonance imaging with metasurfaces. *Adv. Mater.* **28**, 1832–1838 (2016).
87. Kim, I. et al. Nanophotonics for light detection and ranging technology. *Nat. Nanotechnol.* **16**, 508–524 (2021).
88. Kim, J. et al. Metasurface holography reaching the highest efficiency limit in the visible via one-step nanoparticle-embedded-resin printing. *Laser Photonics Rev.* **16**, 2200098 (2022).
89. Schoen, D. T., Holsteen, A. L. & Brongersma, M. L. Probing the electrical switching of a memristive optical antenna by STEM EELS. *Nat. Commun.* **7**, 12162 (2016).
90. Vasista, A. B., Sharma, D. K. & Kumar, G. V. P. Fourier plane optical microscopy and spectroscopy. In Encyclopedia of Applied Physics (ed. Trigg, G. L.) (Weinheim: Wiley-VCH, 2019).
91. Zheng, J. X. et al. Reversible epitaxial electrodeposition of metals in battery anodes. *Science* **366**, 645–648 (2019).
92. Zhou, W. J. et al. Device-quality, reconfigurable metamaterials from shape-directed nanocrystal assembly. *Proc. Natl. Acad. Sci. USA* **117**, 21052–21057 (2020).
93. Lin, M. C. et al. An ultrafast rechargeable aluminium-ion battery. *Nature* **520**, 324–328 (2015).
94. Sherrott, M. C. et al. Experimental demonstration of >230° phase modulation in gate-tunable graphene–gold reconfigurable mid-infrared metasurfaces. *Nano Lett.* **17**, 3027–3034 (2017).
95. Horie, Y. et al. High-speed, phase-dominant spatial light modulation with silicon-based active resonant antennas. *ACS Photonics* **5**, 1711–1717 (2018).
96. Li, Q. T. et al. A Purcell-enabled monolayer semiconductor free-space optical modulator. *Nat. Photonics* **17**, 897–903 (2023).
97. Guarneri, L. et al. Dynamic excitonic beam switching with atomically-thin binary blazed gratings. *Adv. Opt. Mater.* **13**, 2403257 (2025).
98. Wu, P. C. et al. Dynamic beam steering with all-dielectric electro-optic III–V multiple-quantum-well metasurfaces. *Nat. Commun.* **10**, 3654 (2019).
99. Shirmanesh, G. K. et al. Electro-optically tunable multifunctional metasurfaces. *ACS Nano* **14**, 6912–6920 (2020).
100. Mansha, S. et al. High resolution multispectral spatial light modulators based on tunable Fabry-Perot nanocavities. *Light Sci. Appl.* **11**, 141 (2022).
101. Yin, X. H. et al. Beam switching and bifocal zoom lensing using active plasmonic metasurfaces. *Light Sci. Appl.* **6**, e17016 (2017).
102. Choi, C. et al. Metasurface with nanostructured $Ge_2Sb_2Te_5$ as a platform for broadband-operating wavefront switch. *Adv. Opt. Mater.* **7**, 1900171 (2019).
103. Kim, I. et al. Pixelated bifunctional metasurface-driven dynamic vectorial holographic color prints for photonic security platform. *Nat. Commun.* **12**, 3614 (2021).
104. Sisler, J. et al. Electrically tunable space–time metasurfaces at optical frequencies. *Nat. Nanotechnol.* **19**, 1491–1498 (2024).
105. Li, J. X. et al. Addressable metasurfaces for dynamic holography and optical information encryption. *Sci. Adv.* **4**, eaar6768 (2018).
106. de Galarreta, C. R. et al. Nonvolatile reconfigurable phase-change metadevices for beam steering in the near infrared. *Adv. Funct. Mater.* **28**, 1704993 (2018).
107. Ratzsch, J. et al. Electrically switchable metasurface for beam steering using PEDOT polymers. *J. Opt.* **22**, 124001 (2020).
108. Li, Z. et al. Actively switchable beam-steering via hydrophilic/hydrophobic-selective design of water-immersed metasurface. *Adv. Opt. Mater.* **9**, 2100297 (2021).